Experimental and Numerical Study on Sensible Heat Transfer at Droplet/Wall Interactions

E. Teodori[1], P. Pontes[1], A. S. Moita*[1], A. L. N. Moreira[1], A. Georgoulas[2], M. Marengo[2]

[1]IN+ - Center for Innovation, Technology and Policy Research, Instituto Superior Técnico, Universidade de Lisboa, Lisbon, Portugal

[2] Advanced Engineering Centre, School of Computing, Engineering and Mathematics, Cockcroft Building, Lewes Road, University of Brighton, Brighton, UK

*Corresponding author: anamoita@tecnico.ulisboa.pt

Abstract

The present study addresses a detailed experimental and numerical investigation on the impact of water droplets on smooth heated surfaces. High-speed infrared thermography is combined with high-speed imaging to couple the heat transfer and fluid dynamic processes occurring at droplet impact. Droplet spreading (e.g. spreading ratio) and detailed surface temperature fields are then evaluated in time and compared with the numerically predicted results. The numerical reproduction of the phenomena was conducted using an enhanced version of a VOF-based solver of OpenFOAM previously developed, which was further modified to account for conjugate heat transfer between the solid and fluid domains, focusing only on the sensible heat removed during droplet spreading. An excellent agreement is observed between the temporal evolution of the experimentally measured and the numerically predicted spreading factors (differences between the experimental and numerical values were always lower than 3.4%). The numerical and experimental dimensionless surface temperature profiles along the droplet radius were also in good agreement, depicting a maximum difference of 0.19. Deeper analysis coupling fluid dynamics and heat transfer processes was also performed, evidencing a strong correlation between maximum and minimum temperature values and heat transfer coefficients with the vorticity fields in the lamella, which lead to particular mixing processes in the boundary layer region. The correlation between the resulted temperature fields and the droplet dynamics was obtained by assuming a relation between the vorticity and the local heat transfer coefficient, in the first fluid cell i.e. near the liquid-solid interface. The two measured fields revealed that local maxima and minima in the vorticity corresponded to spatially shifted local minima and maxima in the heat transfer coefficient, at all stages of the droplet spreading. This was particularly clear in the rim region, which therefore should be considered in future droplet spreading models.

Keywords

Droplet impact, smooth heated surface, high-speed infrared thermography, VOF, vorticity.

Introduction

Understanding the fluid dynamic and heat transfer mechanisms of droplet impact on heated surfaces is relevant for a wide range of applications, from fire sprinklers to cooling applications. A popular solution for microprocessors cooling is based on spray impingement [1-2]. The elementary representation of a spray composed by arrays of single droplets impacting onto a heated surface is not straightforward in many of the aforementioned applications, but the complexity of the observed phenomena relays on the study of single droplet impacts to understand the basic governing processes. Such approximation is not so far from the real systems for microelectronics cooling, which actually deal with single droplets or with very sparse sprays [1,3]. In many of these applications, liquid phase change is promoted to take advantage of the latent heat of evaporation. However, efficient cooling can be obtained only from sensible heat [4]. Although droplet spreading on heated surfaces has been extensively studied in the literature [4-6], the complex coupling between the fluid dynamics and the heat transfer processes has not yet been completely described. An important limitation in many of the aforementioned studies is that they quantify the heat transfer mainly based on surface temperature measurements at the centre of the impact to the surface, using thermocouples. An alternative approach has been followed more recently by some authors who characterize the spatial and temporal evolution of the temperature field on the surface and/or in the droplet during spreading [7-9]. The resulting data, when carefully processed provide unique information, important to validate more complex numerical models of the droplet/wall interaction process.

In fact, following the pioneering work of [10], who proposed the "Marker and Cell" (MAC) finite difference method to solve the Navier-Stokes equations, other methods have been used to solve numerically the problem of drop impact onto heated surfaces such as the Lagrangian approach [11], the immersed boundary method (IBM) [12] and the Level Set (LS) [13]. In [13], the authors highlight different regions of heat flux along the radial direction of the impacting surface, which can be related with the flow in the lamella. They report that a dip in the heat flux was

noticed close to the droplet rim when the film becomes thinner and thus unable to remove as much heat as the other regions of the spreading droplet. More recently in [6], a VOF based approach is used. The authors were able to solve the conjugate problem of fluid flow and heat transfer during the impact of water droplets onto a heated surface, at surface temperatures low enough to prevent boiling. Liquid properties were a function of local temperature. In [6] a region of high heat flux close to the contact line is reported. The authors related the presence of this region with higher evaporation rates occurring in the contact line.

Despite the completeness of the different models proposed so far in literature, their validation was as aforementioned mostly based on the comparison only with experimental measurements of the surface temperature at the centre of droplet impact. Instead, the present study addresses a more detailed validation process, in which the entire calculated temperature field of the surface in contact with the spreading droplet is compared with the temperature fields obtained experimentally, for different time instants during droplet impact and spreading. The experimental data were gathered combining high-speed IR thermography with high-speed visualization. Main emphasis is put on the sensible heat removed by the droplet and in how the flow field of the droplet can be related with heat and mass transfer phenomena.

Material and methods

Experimental arrangement and methodology

Water droplets formed at the tip of a hypodermic needle and fed by a syringe pump impact on the heated surface by action of gravity. The impact velocity of the droplets is varied by adjusting the height of the needle. The initial droplet diameter is fixed at D_0=2.6±0.1mm. The impact Weber numbers, We=$\rho V_0^2 D_0/\sigma$, where ρ is the liquid density, σ the surface tension and D_0 and V_0 the initial droplet diameter and impact velocity, respectively, range between 24 and 151. The initial surface temperature $T_{W(in)}$ was varied between 333.15K and 373.15K and the ambient temperature was kept at T_{amb}=293±2K. The heated surface is a stainless steel foil electrically heated by copper electrodes clamped on its top. The foil is glued on the top of an insulating thermal glass and the whole assembly is then fixed on a stainless-steel support for an easier positioning. The bottom side of the foil which is used for infrared (IR) thermography is black matt painted to increase the emissivity (ε=0.95). The foil is 20µm thick, 20mm wide and 100mm long.

Wettability is characterized measuring the quasi-static advancing and receding and the static contact angles, using an optical tensiometer (THETA from Attention). The static contact angle, measured by the sessile drop method was θ = 81.7°±1°. The quasi-static advancing and receding angles were used to evaluate the hysteresis of the foil (i.e. the difference between the quasi-static angles), which was always larger than 20°±1° for the hydrophilic foils tested here. The surface is considered to be smooth, with a mean roughness amplitude of the order of 0µm±0.02µm, as evaluated by a Dektak 3 profile meter (Veeco). A detailed description of the experimental procedure taken to characterize the wettability of the surfaces can be found in [14].

An infrared IR-high speed camera (MWIR-InSb from Xenics 179 - ONCA 4696 series) and a high-speed camera (Phantom v4.2) are placed bellow the heated surface and on the side, respectively, to capture simultaneous (but not synchronized) thermal and dynamics images of the impacting droplet.

The IR images were taken at 1000 fps and 150x150px^2, while the high-speed images were taken at 2200 fps and 512X512 px^2. The measurements taken for each experimental condition are averaged from five events, to assure reproducibility of the observed phenomena. Care was taken to assure that the initial surface temperature and wetting conditions were reproducible before each new droplet impact. The impact velocity is evaluated by image post processing, as the vertical displacement of the droplet before impact divided by the time elapsed (i.e. three successive frames of the high-speed video). The initial D_0 and spreading D droplet diameters are also evaluated from image post-processing, with a home-made routine, as in [15], being then used to determine the spreading ratio D/D_0. The radial temperature profiles were obtained after post processing the IR images using a home-made MatLab code, which converts the raw IR images to temperature data.

To eliminate the effect of the initial surface temperature, which is varied within the experimental campaign, a non-dimensional temperature is considered, which is defined as T^*:

$$T^* = \frac{[T_W(r,t) - T_{amb}]}{[T_W(in) - T_{amb}]} \tag{1}$$

where $Tw(r,t)$ is the temperature of the bottom of the foil. at time t after droplet impact and at a distance r from the center of the droplet (point of impact). Temperature profiles are obtained by plotting T^* as a function of the non-dimensional radial distance $r/D0$.

The imposed volumetric heat flux q''' is evaluated as:

$$q''' = \frac{V \cdot I}{e \cdot L \cdot W} \tag{2}$$

being V and I the applied voltage and resulting current passing through the stainless steel foil. e, L and W are the thickness, length and width of the foil, respectively.

Measurement uncertainties

The main uncertainties associated to droplet dynamics are summarized in Table 1, while Table 2 depicts the uncertainties associated to the main parameters used to describe the heat transfer process at droplet/wall interaction. These uncertainties are evaluated following Abernethy *et al.* [16]. For the quantities taken from image analysis, the uncertainties depend on the definition of the boundaries of the droplet in pixels (±2pixels in the worst case scenario). More details can be found in Valente *et al.* [17].

Table 1. Uncertainties of the main parameters used to describe droplet dynamics.

Parameter	Uncertainties (rel. or abs)
Droplet diameter before impact D_o [mm] Spreading diameter D $[mm]$	$U_D = \pm 160 \mu m$ $U_{D_o} = \pm 160 \mu m$
Spreading ratio D/D_o[-]	$u_{D/D_o} max = \pm 37\% \ at \ (D/D_o = 0.17)$ $u \, D/D_o \ mim = \pm 7\% \ at \ (D/D_o = 3.86)$
Impact velocity $V_0 [m/s]$	$U_{V_o} = 0.08 \ [m/s]$
Weber number We[-]	$u_{We} \ max = \pm 15\% \ at \ (We = 24)$ $u_{We} \ mim = \pm 8\% \ at \ (We = 151)$

Table 2. Uncertainties of the main parameters used to describe the heat transfer process during droplet spreading.

Parameter	Uncertainties U (rel. or abs)
Temperature T[K]	$U_T = \pm 1K$
Temperature difference ΔT [K]	$U_{\Delta T} = \pm 1.4K$ $u_{\Delta T} max = \pm 14\% \ at \ (\Delta T = 10 \ K)$ $u_{\Delta T} min = \pm 1.7\% \ at \ (\Delta T = 78 \ K)$
Non-dimensional temperature T*[-]	$U_{T^*} max = \pm 0.04 \ at \ (T^* = 1)$ $U_{T^*} min = \pm 0.02 \ at \ (T^* = 0.3)$ $u_{T^*} max = \pm 6\% \ at \ (T^* = 0.3)$ $u_{T^*} max = \pm 4\% \ at \ (T^* = 1)$
Imposed volumetric heat flux $q''' [W/m^3]$	$u q''' \ max = \ \pm 12\% \ at (q''' = 6.5 \cdot 10^6 \ [W/m^3])$
Radial distance r [mm]	$U_r = \pm 200 \ \mu m$

Numerical methodology

A VOF-based approach was used for interface capturing, with an enhanced VOF model implemented in OpenFOAM CFD Toolbox [18]. This enhanced model is coupled with the energy equation that accounts for two-phase heat transfer in the liquid domain and with transient heat conduction in a solid domain. In the VOF method, a volume fraction field α identifies the volume of liquid within a cell. The volume of the gaseous phase is therefore given as (1- α). The value of α is 1 inside the pure liquid cells, 0 in the pure gas cells and between 0 and 1 in the cells containing the interface area. This procedure allows using a single set of continuity and momentum equations for the entire flow domain:

Continuity equation

$$\Delta \cdot \vec{U} = 0 \tag{3}$$

Momentum equation

$$\frac{\partial \rho_b}{\partial t} + \nabla \cdot \left(\rho_b \vec{U}\vec{U}\right) = -\nabla p + \nabla \cdot \mu_b\left(\nabla \vec{U} + \nabla \vec{U}^T\right) + \rho_b f + F_s \tag{4}$$

Interface advection

$$\frac{\partial \alpha}{\partial t} + \nabla \cdot \left(\alpha \vec{U}\right) = 0 \tag{5}$$

Energy equation

$$\rho_b c_{p_b} \frac{\partial T}{\partial t} + \nabla \cdot \left(\vec{U} \rho_b c_{p_b} T\right) = \nabla \cdot (k_b \nabla T) \tag{6}$$

Here, $\vec{U}$ stands for the velocity of the liquid, p the pressure and T the temperature. Gravitational forces are represented as f while F_s represents the volumetric surface tension forces. k_b, ρ_b, μ_b and c_{p_b} are the thermal conductivity, the density, the dynamic viscosity and the heat capacity of the bulk liquid, respectively. These are calculated as:

$$\gamma_b = \gamma\alpha + \check{\gamma}(1 - \alpha) \tag{7}$$

The energy equation for the liquid (3) does not account for evaporation or diffusion of the liquid phase in the gas phase. This approximation is considered valid in the relatively small time scale that is investigated here. This is in agreement with the results reported, for instance by [12-13, 19-20]. The Continuum Surface Force (CFS) method proposed in [21] was used to model the surface tension as a volumetric force. The following equations stand:

$$F_s = \sigma\kappa(\nabla\alpha) \tag{8}$$

$$\kappa = \nabla\left(\frac{\nabla\alpha}{|\nabla\alpha|}\right) \tag{9}$$

where κ is the curvature of the interface and σ is the tension of the interface. Heat is transported only by conduction in the solid. The governing energy equation is therefore given as:

$$\rho_s c_{v_s} \frac{\partial T_s}{\partial t} - \nabla \cdot (k_s \nabla T_s) = q_V''' \tag{10}$$

where the subscript "s" indicates that the properties are of the solid only. The volumetric heat source is represented as q_V''' $[W/m^3]$ and is homogenously distributed in the solid domain.

Numerical domain and boundary conditions

The set of equations described above is solved in an axisymmetric domain, represented by a 5°. An 8X8mm^2 fluid domain in the X-Y plane was chosen to avoid the influence of the boundaries in the fluid flow. The dimensions of the solid domain were 8X0.020mm^2, (20µm thickness of the heated foil). The mesh consisted of 640000 hexahedral cells in the fluid domain and 4000 in the solid domain. In the fluid domain, the mesh progressively coarsens away from the initial droplet position by a grading factor of 5 in both X and Y directions (last to first cell dimension in each direction is equal to 5). This leads to a minimum cell size of 4µm and a maximum cell size of 20µm. These cell dimensions assure the solution to be mesh independent. Before each simulation, an arbitrary thermal boundary layer was patched in the domain to facilitate the initial convergence of the coupling between the solid and liquid temperatures. A droplet with the same diameter and velocity as in the experimental conditions was patched as well, at the time instant just before it contacts with the heated surface. The solid was considered as a volumetric heat source. Constant contact angle was assumed between the fluid and the solid with a value of θ=81.7º, following the experimentally measured value.

The PISO algorithm is used for pressure-velocity coupling, considering an Eulerian scheme for the time derivative and a Gauss linear for the gradient divergence as well as for the Laplacian terms. The flow field is assumed to be laminar. The conjugate heat transfer problem is solved by iteratively coupling of the temperature field and the heat flux between the solid and liquid domains, following a procedure similar to that reported in [22]. The simulations

were run with a variable calculation time step to assure a constant Courant number of 0.2. Numerical reproduction of some of the experimental results was performed to benchmark the code. An overview of the conducted simulations is reported in Table 3.

Table 3 Thermo-physical properties of the fluids and solid used in the performed simulations. ρ, C_p, k_l, ν and σ and the liquid density, specific heat, thermal conductivity, kinematic viscosity and surface tension, respectively.

	ρ[kg/m^3]	c_p[J/kgK]	k_l [W/mK]	ν [m^2/s]	σ[N/m]
Air	1	1006.4	0.025874	0.0000148	-
Water	1000	4184	0.59844	0.000001	0.007
Stainless Steel	7880	477	18	-	-

Results and discussion

For comparative purposes between the experimental data and the numerical results, Figure 1 depicts a sequence of high-speed images, the corresponding numerical simulations (side view of the droplet) and IR images of the surface (bottom view) taken during the spreading of a water droplet at We=24 on the stainless steel foil, initially heated at $T_{W(in)}$=353.15K. The figure anticipates a good agreement between the experimental data and the numerical predictions, regarding the shape of the spreading droplet and the temperature field. A quantitative comparison is shown in Figure 2, which depicts the temporal evolution of the calculated and measured spreading factors.
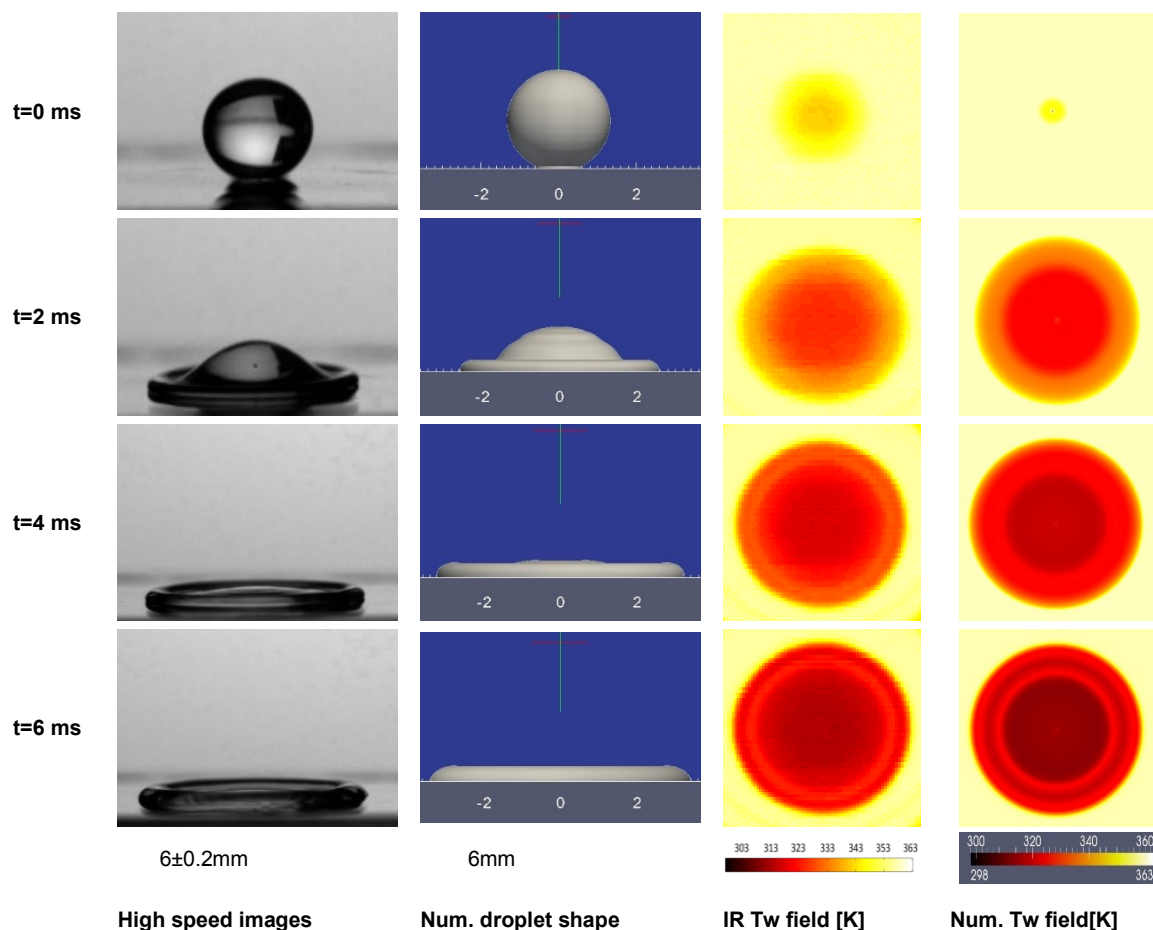

| High speed images | Num. droplet shape | IR Tw field [K] | Num. Tw field[K] |

Figure 1. Qualitative comparison between high-speed images, the corresponding numerical simulations (side view of the droplet), IR images of the surface (bottom view) and the corresponding calculated temperature field. The comparative analysis is performed for various time instants after the impact of a water droplet at We=24 on the stainless steel foil initially heated at $T_{w(in)}$=353.15K.

Figure 2 supports the excellent agreement between the numerical and the experimental results. At the first stage of spreading (t<2ms) the observed discrepancies are mostly due to the uncertainty

associated to the definition of the instant of impact, t=0ms. Considering the temporal resolution of the high-speed recordings, the actual impact can occur up to 0.5ms before or after the frame chosen to establish the instant of impact. In the numerical simulation, on the other hand, the time resolution of the post-processed data is 0.1ms. Hence, particularly at these early stages after impact, the differences between the numerical and the experimental results can be considerable. However, as the spreading factor increases and, therefore the time after impact increases, the difference between numerical and experimental results reduces. At the maximum spreading diameter, the maximum difference between the experimentally measured and the numerically predicted spreading factor is 3.4%.
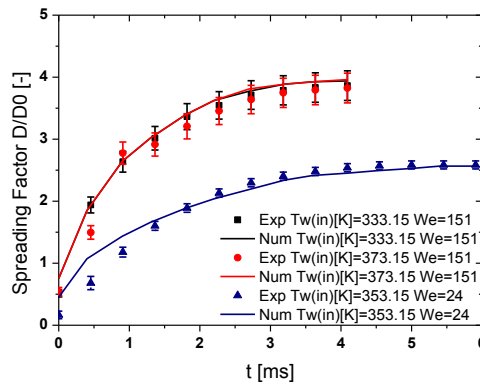

Figure 2. Temporal evolution of the calculated and measured spreading factors for the impact conditions of Figure 1.

A preliminary relation can be established between droplet dynamics and the heat transfer processes, comparing dimensionless surface temperature profiles T*, as defined in equation (1), along the dimensionless radial distance r/D_0 at different instants after impact. Such profiles are depicted in Figure 3 for two different Weber numbers, We=24 and We=151 and for three different initial surface temperatures, namely $T_{W(in)}$=333.15, 353.15 and 373.15K.
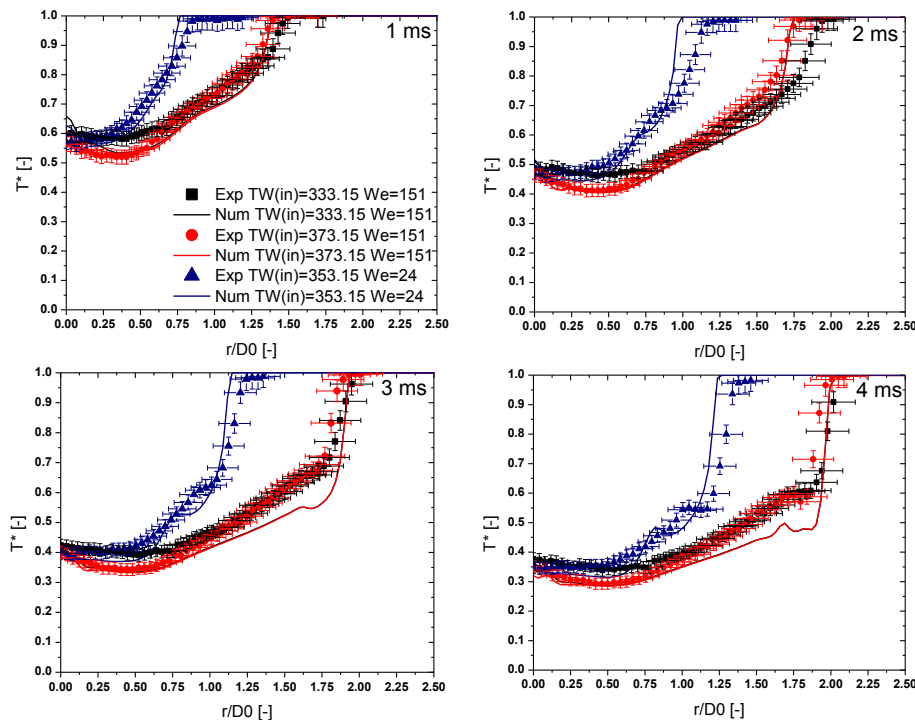

Figure 3. Dimensionless temperature profiles along the dimensionless radial distance for 1,2,3 and 4 ms after impact, for We=24 and We=151 and for three different initial surface temperatures, namely $T_{W(in)}$=333.15, 353.15 and 373.15K..

Given that the maximum spreading diameter for We=151 is reached 4ms after impact, the results are only presented and discussed up to this time instant. The figure clearly evidences a very good agreement between the experimental results and the numerical predictions, particularly towards the center of the impact ($r/D_0 \approx 0$), for all the conditions tested. For instance, for We=151, in the range of $r/D0 < 1.2$ the maximum difference between the numerical and experimental profiles T* is 11%. For We=24 in the range $r/D_0 < 0.5$, the maximum difference in T* is 5%. These differences are negligible, being within the uncertainty of the experimental measurements. Some discrepancies are however noticeable at higher values of r/D_0, in the region of the rim and of the gas-liquid-solid contact line. The contact line can be identified at the maximum value of $r/D0$ before T*=1. T*=1 means that any temperature variation occurs on the surface, i.e. the surface is not wetted yet by the droplet. On the other hand, close to the contact line, a steep temperature variation occurs. Consequently, any small difference between the measured and the calculated position of the contact line can lead to substantial differences between the measured and the numerically predicted T* (up to 30% of the experimentally measured value). The rim is identified by the non-monotonic decrease in the temperature along r/D_0. Both experimental and numerical results show that the temperature does not decrease with increasing r/D_0, but local maxima and minima occur instead. This is particularly evident at 3 and 4ms after impact, for all the We numbers tested. Here, the maximum difference between the experimental and the numerical values of T* is 16% for We=151 at 4ms after impact and at r/D_0=1.75 and 11% for We=24 at 4ms after impact and at $r/D_0 \approx 1$. Within the rim, the various heat transfer mechanisms occur in extremely small temporal and spatial scales. Hence, matching the experimental and the numerically calculated temperatures strongly depends on the relation between the instrumental and the numerical resolution. In the numerical simulations, the mesh size varies between 4µm up to 20µm and the reported numerical profiles were sampled with a sampling size of 80µm. The temporal resolution was 0.1ms. On the other hand, the spatial resolution of the IR camera was of 110µm/px, the temporal resolution of 483 the IR camera was 1ms and the integration time was 200 µs. This means that the temperature variation captured by the IR camera could be integrated within a larger temporal-spatial domain and thus the resulting values can be spatially damped or temporally delayed up to a certain amount. Despite these limitations, the trend of the temperature profiles is very well captured by the numerical simulations.

Three typical characteristic regions can be identified in the temperature profile: 1) The first is a steep increase in temperature at the entrance to the rim, 2) the second is the appearance of a temperature local minimum in the region within the rim and 3) the third is a steep decrease in temperature, observed near the contact line (Figure 4).
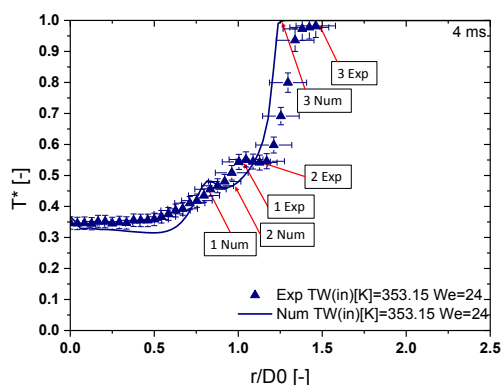

Figure 4. Measured and calculated temperature distribution along the dimensioless radial distance for a droplet impacting at We=24 on the surface initially heated at TW8in)=353.15K. 1, 2 and 3 identify the 3 characteristic regions of the temperature profile.

These trends differ from those reported by for e.g. [20], who measured a constant temperature increase along the droplet radius due to the decreased convective heat transfer in the outward fluid direction. However, numerically, a temperature distribution similar to that obtained here was reported for instance by [13]. These discrepancies arising from experimental and numerical studies can be explained by further detailing the fluid dynamics within the droplet, specifically at the lamella and within the rim, in the attempt to relate the fluid dynamic behaviour with the heat transfer process. Such detailed study was performed for the impact of a droplet at We =24 and $T_{W(in)}$=353.14K. The analysis performed, which is not presented here due to paper length constrains clearly evidenced large local temperature variations, particularly within the rim, where adverse flow can occur. In fact, there is a complex structure of vortices within the rim and in the lamella, which can be related with the local heat

transfer coefficients and with the aforementioned temperature variations. These vortex structures promote the mixing in the thermal boundary layer, which affects particularly the heat transfer process at the liquid-solid interface. In line with this, the vorticity was evaluated and correlated with the heat transfer coefficient at the centre of the first layer of fluid cells i.e. at a vertical distance of 2µm from the liquid-solid interface. The correlation between the resulted temperature field and the droplet dynamics was obtained by assuming a relation between the vorticity and the local heat transfer coefficient, in the first fluid cell i.e. near the liquid-solid interface. The two measured fields revealed that local maxima and minima in the vorticity correspond to spatially shifted local minima and maxima in the heat transfer coefficients, at all stages of the droplet spreading. This was particularly clear in the rim region.

Conclusions

This work concerns a detailed analysis of the spreading process of a water droplet on a heated smooth surface, coupling the fluid dynamics with the heat transfer processes. The experimental analysis comprises the combination of high-speed infrared thermography with high-speed imaging evaluate the spreading behaviour (e.g. the spreading ratio) together with detailed surface temperature fields along the spreading radius, during the spreading. The numerical simulations were conducted using an enhanced version of a VOF-based solver of OpenFOAM previously developed, which was further modified to account for conjugate heat transfer between the solid and fluid domains, focusing only on the sensible heat removed during droplet spreading.

An excellent agreement is observed between the temporal evolution of the experimentally measured and the numerically predicted spreading factors. The numerical and experimental dimensionless surface temperature profiles along the droplet radius were also in good agreement. The temperature fields revealed a non-homogenous cooling of the surface which was related with droplet dynamics. Hence, the coupled analysis of the fluid dynamics and heat transfer processes within the lamella evidenced a strong correlation between maximum and minimum temperature values and heat transfer coefficients with the vorticity fields in the lamella, which lead to particular mixing processes in the boundary layer region, at all stages of droplet spreading. This was particularly clear in the rim region, which therefore should be always accounted for in droplet spreading models.

Acknowledgements

References

[1] Kim., J., 2007, Int. J. Heat Fluid Flow, 28, pp. 253-267.
[2] Panão, M., Guerreiro, J. and Moreira, A.L.N., 2012, Int. J. Heat Mass Transf. 55, pp. 2854-2863.
[3] Moita, A.S. and Moreira, A.L.N., 2012, Experiments in Fluids, 52, pp. 679-695.
[4] Pasandideh-Fard, M., Aziz, S., Chandra, S. and Mostaghimi, J., 2001, Int. J. Heat Fluid Flow, 22, pp. 201-210.
[5] Haley W., Hartley, J. and Abdel-Khalik, S., 2001, Int. J. Heat Mass Transf., 44, pp. 3869-3881, 2001.
[6] Strotos G., Aleksis G., Gavaises M., Nikas, K.-S., Nikolopoulos, N. and Theodorakakos, A., 2011, Int. J. Thermal Sci., 50, pp. 698–711.
[7] Tartarini, P., Corticelli, M.A. and Tarozzi, L., 2009, Appl. Thermal Eng., 29, pp. 1391-1397.
[8] Girard, F., Antoni, M. and Sefiane, K., 2010, Langmuir, 26, pp. 4576-4580.
[9] Gradeck, M., Seiler, N., Ruyer, P. and Maillet, D., 2013, Exp. Thermal Fluid Sci., 47, pp. 14-25.
[10] Harlow, F. H. and Shannon, J. P., 1967, J. Appl. Phys., 38, pp. 3855–3866.
[11] Zhao, Z., Poulikakos, D. and Fukai, J., 1996, Int. J. Heat Mass Transf., 39, pp. 2771–2789.
[12] Francois, M. and Shyy, W., 2003, Numer. Heat Transf. Part B Fundam., 44, pp. 101–118.
[13] Healy, W.M., Hartley, J.G. and Abdel-Khalik, S.I., 2001, Int. J. Heat Mass Transf., 44, pp. 3869–3881.
[14] Pereira P., Moita, A. S., Monteiro, G. and Prazeres, D.M.F., 2014, J. Bionic Eng., 11(3), pp. 346-359.
[15] Moita, A.S., Herrmann, D. and Moreira, A.L.N., 2015, Appl. Thermal Eng., 88, pp. 33-46.
[16] Abernethy, R., Benedict, R. and Dowdell, R., 1985, J. Fluids Eng. 107, pp. 161–164.
[17] Teodori, E., Valente, T., Malavasi, I., Moita, A.S., Marengo, M. And Moreira, A.L.N., 2017, Applied Thermal Eng., 115, pp. 1424-1437.
[18] Georgoulas, A., Andredaki, M. and Marengo, M., 2017, Energies, 10(3), pp. 1-35. ISSN 1996-1073.
[19] Francois, M. and Shyy, W., 2003, Numer. Heat Transf. Part B Fundam., 44, pp. 119–143.
[20] Jackson, R.G., Kahani, M., Karwa, N., Wu, A., Lamb, R., Taylor, R. and Rosengarten, G. 2014, J. Phys. Conf. Ser., 525, p. 12024.
[21] Brackbill, J., Kothe, D., and Zemach, C., 1992, J. Comput. Phys., 100, pp. 335–354.
[22] Kunkelmann, C. Numerical Modeling and Investigation of Boiling Phenomena, Technische Universitaet Darmstadt, 2011.